Quantum chemical study of the electronic structures of MnC2−/0 clusters and interpretation of the anion photoelectron spectra

ARTICLE *in* CHEMICAL PHYSICS LETTERS · JUNE 2013

Impact Factor: 1.9 · DOI: 10.1016/j.cplett.2013.04.079

3 AUTHORS, INCLUDING:

Van Tan Tran
chemistry
15 PUBLICATIONS **96** CITATIONS
SEE PROFILE

Marc F A Hendrickx
University of Leuven
28 PUBLICATIONS **248** CITATIONS
SEE PROFILE

Chemical Physics Letters 575 (2013) 46–53

Contents lists available at SciVerse ScienceDirect

Chemical Physics Letters

journal homepage: www.elsevier.com/locate/cplett

Quantum chemical study of the electronic structures of $MnC_2^{-/0}$ clusters and interpretation of the anion photoelectron spectra

Van Tan Tran [a], Christophe Iftner [b], Marc F.A. Hendrickx [a,*]

[a] Afdeling Kwantumchemie en Fysicochemie, Departement Chemie, Katholieke Universiteit Leuven, Celestijnenlaan 200F, B-3001 Heverlee-Leuven, Belgium
[b] Laboratoire de Chimie et Physique Quantiques, IRSAMC, Université Paul Sabatier, 118 route de Narbonne, 31062 Toulouse Cedex 09, France

ARTICLE INFO

Article history:
Received 19 March 2013
In final form 30 April 2013
Available online 13 May 2013

ABSTRACT

Cyclic and linear $MnC_2^{-/0}$ clusters have been theoretically studied. The $^7A_1$ and $^6A_1$ states of the cyclic isomer are calculated to be the ground states of the anionic and neutral cluster, respectively. All observed bands in the experimental photoelectron spectra of MnC_2^- could be assigned to the cyclic isomer. The X band is ascribed to an ionization during which an electron is detached from a nonbonding 4s4p hybrid orbital. The higher bands in the spectra are the result of ionization processes in which an electron from the nonbonding HOMO of the C_2^{2-} ligand is removed.

1. Introduction

The interaction between transition metals and carbon has received a good deal of attention during the past decades. In particular, transition metal carbide clusters are relevant to new materials such as metallo-carbohedrenes (met-cars) and metallofullerene [1–5]. It is therefore no surprise that extensive experimental and theoretical investigations on different kinds of small transition metal carbide clusters have been carried out for the purpose to understand the growth mechanism of these nanomaterials and to obtain an insight into their physical and chemical properties [6–14]. Furthermore, the complicated electronic structure of transition metal containing clusters represents a challenging subject for theoretical chemists [10,15–22].

For the smaller transition metal carbide clusters MC_2 (M = Sc, V, Cr, Mn, Fe, and Co), the anion photoelectron spectra were systematically measured with photon energies of 532 and 355 nm [9]. These spectra contain however insufficient information about the geometric and electronic structures of both the anionic and neutral clusters, and therefore need to be investigated by computational quantum chemical techniques. In the past, assignments of anion photoelectron spectra of vanadium, chromium, iron and cobalt dicarbide clusters were proposed by using TDDFT (time-dependent density functional theory) at the B3LYP/LANL2DZ level [23]. CrC_2^- photoelectron spectra have been assigned at the DFT and CCSD(T) levels [14]. Additionally, due to the expected near-degeneracy effects in the wavefunctions their electronic states, multireference wavefunction methods such as CASPT2 (complete active-space second-order perturbation theory) and MRCI (multireference configuration interaction) were applied to investigate the low-lying structures of some of these clusters [10,15–20].

For the $MnC_2^{-/0}$ clusters, to our knowledge, the anion photoelectron spectroscopy spectra have not been interpreted at any level of theory yet. Theoretical work in relation to the title clusters is limited to the investigation of the geometric and electronic structures of $MnC_2^{0/+}$ with various computational methods ranging from single-determinant DFT, QCISD (quadratic configuration interaction including single and double excitations) and CCSD(T) (coupled-cluster with single and double and perturbative triple excitations) to multireference CASSCF (complete active-space self consistent field) and MRCI [21,22]. For the MnC_2 cluster, the electronic and vibrational properties of both of the cyclic and linear isomers were studied [21,22]. The obtained results showed that the ground state of this cluster is $^6A_1$ of the cyclic isomer. The $^6\Sigma^+$ state of the linear isomer was calculated to be 0.64 eV and 0.87 eV less stable at the CCSD(T) and MRCI level, respectively.

In this letter we have utilized the B3LYP, CASPT2 and RCCSD(T) methods to investigate the geometric and electronic structures of $MnC_2^{-/0}$ clusters with the principle aim to propose assignments for the observed bands in the anion photoelectron spectra. Our state-of-the-art calculations employ large basis sets to include the outer-core electrons (3s and 3p) of manganese into the electron correlation treatment. Also Franck–Condon factors, which have previously been demonstrated to be quite useful to study the vibrational progressions of the anion photoelectron spectra of iron-oxide and iron-sulfide clusters [24–26], are also calculated for these clusters.

2. Computational method

Two isomers with cyclic and linear $MnC_2^{-/0}$ structures are studied in this letter. From previous calculations and our DFT

* Corresponding author.
E-mail address: marc.hendrickx@chem.kuleuven.be (M.F.A. Hendrickx).

0009-2614/$ - see front matter © 2013 Elsevier B.V. All rights reserved.
http://dx.doi.org/10.1016/j.cplett.2013.04.079

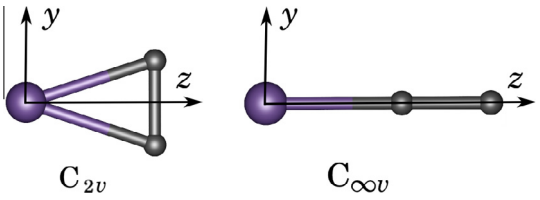

Figure 1. Coordinate systems employed for the cyclic $MnC_2^{-/0}$ and linear $MnC_2^{-/0}$ clusters.

calculations it is clear that the cyclic isomer has a C_2 moiety side-on bound to manganese, while for the linear isomer it is end-on bound to the metal (see Figure 1). These two isomers have C_{2v} and $C_{\infty v}$ symmetries. Because only Abelian point groups are implemented in the employed software packages, the C_{2v} symmetry is used throughout all calculations. The cyclic isomer is placed in the YZ plane and the twofold axis coincides with the *Z* axis. As conventional, the linear isomer is placed along the *Z* axis.

Our investigation started by performing DFT geometry optimizations for different spin multiplicities in the range from singlet to octet for both the cyclic and linear $MnC_2^{-/0}$ isomers by using the spin-unrestricted scheme and without any spatial symmetry constraints. As has been intensely tested for $MC_2^{0/+}$ (M = Sc–Zn) clusters [21,22], the hybrid B3LYP [27–29] functional performs adequately and was consequently utilized in this letter. Harmonic vibrational analyses were also performed in order to find out whether the obtained stationary points are local minima on the potential energy surfaces. Subsequently, for the lower energy structures spatial symmetry was introduced with the purpose to access more low-lying electronic states. The def2-QZVP basis sets are utilized for both manganese and carbon atoms [30]. All the B3LYP calculations were carried out with the MOLPRO 2009 program package [31]. The DFT equilibrium structures and harmonic vibrational frequencies for the spectroscopic relevant low-lying states allowed to derive the multidimensional Franck–Condon factors for which the MOLFC code was employed [32].

The molecular orbitals needed for the CASPT2 calculations are obtained by CASSCF with an active space of 16 or 15 electrons in 14 orbitals. This active space, which includes all the valence orbitals of Mn (3d and 4s) and C (2s and 2p), is somewhat larger than the active space of 13 orbitals as used in the previous work [21,22] and is sufficiently flexible to describe all low-lying states of $MnC_2^{-/0}$. ANO-RCC basis sets with contractions [10s10p8d6f4g2h] and [8s7p4d3f2g] were employed for manganese and carbon, respectively [33,34]. Scalar-relativistic effects were included by using the Douglas-Kroll Hamiltonian [35–37]. For the CASPT2 calculations, the electrons of the outer-core (3s and 3p) orbitals of manganese were additionally correlated. An imaginary shift of 0.1 was applied in the perturbation step to remove intruder states. Structures of all relevant low-lying states were optimized at the CASPT2 level. All CASPT2 calculations were carried out with the MOLCAS 7.6 software package [38].

RCCSD(T) calculations were performed with MOLPRO 2009 [31]. A ROHF (restricted open-shell Hartree–Fock) calculation, which avoids spin contamination problems of the open-shell states, was performed first to produce the leading configuration wavefunction for the subsequent RCCSD(T) step. Aug-cc-pwCVnZ-DK[39] and aug-cc-pVnZ-DK[40] ($n = T$ and 5) basis sets were employed for manganese and carbon, respectively. Geometries of the low-lying states of $MnC_2^{-/0}$ were optimized with the triple-ζ basis sets. Based on these equilibrium structures, single-point calculations with quintuple-ζ basis sets were also carried out with the aim to improve the energies. Besides the valence electrons of Mn (3d and 4s) and C (2s and p) also the outer-core electrons (3s and 3p) of Mn were correlated. Scalar-relativistic effects were again included by using the Douglas-Kroll Hamiltonian to second-order.

3. Results and discussion

Structural parameters, relative energies and harmonic frequencies of the low-lying states of cyclic and linear $MnC_2^{-/0}$ as calculated at B3LYP/def2-QZVP are collected in the upper part of Table 1. For the neutral cluster, our B3LYP calculations confirm the previous

Table 1
Structural parameters, relative energies, and harmonic vibrational frequencies for the relevant states of $MnC_2^{-/0}$ as calculated by B3LYP, CASPT2, and RCCSD(T). (a) For the RCCSD(T) results, the structures were optimized with the triple-ζ basis sets, whereas the relative energies were obtained by single-point calculations with quintuple-ζ basis sets. (b) At the B3LYP level the leftmost value for each state corresponds to the frequency of the Mn–C_2 asymmetric stretching mode of the cyclic isomer or of the MnCC asymmetric bending mode of the linear isomer. The last two values correspond to the frequencies of the Mn–C_2 and C–C symmetric stretching modes.

Method	Cluster	State	Mn–C, C–C (Å)	RE (eV)	Frequency[(b)] (cm^{-1})
B3LYP	Cyclic – MnC_2^-	$^5A_1$	2.079, 1.267	0.30	160, 470, 1800
		$^7A_1$	2.094, 1.264	0.00	284, 474, 1815
	Cyclic-MnC_2	$^6A_1$	1.980, 1.272	1.87	367, 566, 1758
		$^8A_1$	2.247, 1.258	2.93	202, 383, 1849
	Linear – MnC_2^-	$^5A_1(^5\Sigma^+)$	1.888, 1.260	0.24	145, 483, 1875
		$^7A_1(^7\Sigma^+)$	1.946, 1.262		
	Linear-MnC_2	$^6A_1(^6\Sigma^+)$	1.826, 1.268		
CASPT2	Cyclic – MnC_2^-	$^5A_1$	2.060, 1.283	0.65	
		$^7A_1$	2.075, 1.285	0.00	
	Cyclic-MnC_2	$^6A_1$	1.967, 1.284	1.98	
		2^6A_1	2.067, 1.292	2.70	
		$^8A_1$	2.215, 1.274	2.73	
	Linear – MnC_2^-	$^5A_1(^5\Sigma^+)$	1.862, 1.273	0.70	
		$^7A_1(^7\Sigma^+)$	1.941, 1.273	0.37	
	Linear-MnC_2	$^6A_1(^6\Sigma^+)$	1.986, 1.258	2.74	
		$^8A_1(^8\Sigma^+)$	2.036, 1.241	3.01	
RCCSD(T)[(a)]	Cyclic – MnC_2^-	$^7A_1$	2.105, 1.281	0.00	
	Cyclic-MnC_2	$^6A_1$	2.001, 1.287	2.18	
		$^8A_1$	2.244, 1.275	2.93	
	Linear – MnC_2^-	$^5A_1(^5\Sigma^+)$	1.862, 1.274	0.94	
		$^7A_1(^7\Sigma^+)$	1.967, 1.275	0.39	
	Linear-MnC_2	$^6A_1(^6\Sigma^+)$	1.900, 1.273	2.83	
		$^8A_1(^8\Sigma^+)$	2.063, 1.243	3.33	

Table 2
CASPT2 vertical relative energies of $MnC_2^{-/0}$ as calculated with the optimized geometries of the $^7A_1$ ground states of cyclic and linear MnC_2^-.

State	Leading configuration	VDE (eV)	Orb.	Expt. (eV)
Cyclic MnC_2^-				
$^5A_1$	$9a_1^2 10a_1^2 11a_1^1 12a_1^0 3b_1^2 4b_1^1 4b_2^2 5b_2^1 6b_2^0 1a_2^1$	0.65		
$^5A_2$	$9a_1^2 10a_1^1 11a_1^1 12a_1^0 3b_1^2 4b_1^1 4b_2^2 5b_2^1 6b_2^0 1a_2^2$	1.63		
$^5B_1$	$9a_1^2 10a_1^1 11a_1^1 12a_1^0 3b_1^2 4b_1^2 4b_2^2 5b_2^1 6b_2^0 1a_2^1$	1.52		
$^5B_2$	$9a_1^2 10a_1^1 11a_1^0 12a_1^1 3b_1^2 4b_1^1 4b_2^2 5b_2^2 6b_2^0 1a_2^1$	2.21		
$^7A_1$	$9a_1^2 10a_1^1 11a_1^1 12a_1^1 3b_1^2 4b_1^1 4b_2^2 5b_2^1 6b_2^0 1a_2^1$	0.00		
$^7A_2$	$9a_1^2 10a_1^1 11a_1^1 12a_1^1 3b_1^1 4b_1^1 4b_2^2 5b_2^2 6b_2^0 1a_2^1$	3.97		
$^7B_1$	$9a_1^2 10a_1^1 11a_1^1 12a_1^2 3b_1^1 4b_1^1 4b_2^2 5b_2^1 6b_2^0 1a_2^1$	3.50		
$^7B_2$	$9a_1^2 10a_1^1 11a_1^1 12a_1^0 3b_1^2 4b_1^1 4b_2^2 5b_2^1 6b_2^1 1a_2^1$	2.35		
Cyclic MnC_2				
$^6A_1$	$9a_1^2 10a_1^1 11a_1^1 12a_1^0 3b_1^2 4b_1^1 4b_2^2 5b_2^1 6b_2^0 1a_2^1$	2.10	$12a_1$	2.12 (X)
2^6A_1	$9a_1^1 10a_1^1 11a_1^1 12a_1^1 3b_1^2 4b_1^1 4b_2^2 5b_2^1 6b_2^0 1a_2^1$	2.89	$9a_1$	2.86 (A)
$^6A_2$	$9a_1^1 10a_1^1 11a_1^0 12a_1^1 3b_1^2 4b_1^1 4b_2^2 5b_2^1 6b_2^0 1a_2^2$	5.81		
$^6B_1$	$9a_1^2 10a_1^1 11a_1^1 12a_1^1 3b_1^2 4b_1^0 4b_2^2 5b_2^1 6b_2^0 1a_2^1$	3.77		
$^6B_2$	$9a_1^2 10a_1^1 11a_1^1 12a_1^1 3b_1^2 4b_1^1 4b_2^2 5b_2^0 6b_2^0 1a_2^1$	4.89		
$^8A_1$	$9a_1^1 10a_1^1 11a_1^1 12a_1^1 3b_1^2 4b_1^1 4b_2^2 5b_2^1 6b_2^0 1a_2^1$	2.87	$9a_1$	3.06 (B)
$^8A_2$	$9a_1^1 10a_1^1 11a_1^1 12a_1^1 3b_1^1 4b_1^1 4b_2^2 5b_2^2 6b_2^0 1a_2^1$	7.56		
$^8B_1$	$9a_1^2 10a_1^1 11a_1^1 12a_1^1 3b_1^1 4b_1^1 4b_2^2 5b_2^1 6b_2^0 1a_2^1$	4.20		
$^8B_2$	$9a_1^2 10a_1^1 11a_1^1 12a_1^1 3b_1^2 4b_1^1 4b_2^1 5b_2^1 6b_2^0 1a_2^1$	5.74		
Linear MnC_2^-				
$^5A_1$	$10a_1^2 11a_1^1 12a_1^2 13a_1^0 3b_1^2 4b_1^1 5b_1^0 3b_2^2 4b_2^1 1a_2^1$	0.74		
$^5A_2$	$10a_1^2 11a_1^0 12a_1^1 13a_1^1 3b_1^2 4b_1^1 5b_1^0 3b_2^2 4b_2^1 1a_2^2$	3.16		
$^5B_1$	$10a_1^2 11a_1^1 12a_1^1 13a_1^2 3b_1^2 4b_1^0 5b_1^0 3b_2^2 4b_2^1 1a_2^1$	2.35		
$^5B_2$	$10a_1^2 11a_1^1 12a_1^1 13a_1^2 3b_1^2 4b_1^1 5b_1^0 3b_2^2 4b_2^0 1a_2^1$	2.37		
$^7A_1$	$10a_1^2 11a_1^1 12a_1^1 13a_1^1 3b_1^2 4b_1^1 5b_1^0 3b_2^2 4b_2^1 1a_2^1$	0.37		
$^7A_2$	$10a_1^1 11a_1^1 12a_1^1 13a_1^1 3b_1^2 4b_1^1 5b_1^0 3b_2^2 4b_2^1 1a_2^2$	3.16		
$^7B_1$	$10a_1^2 11a_1^1 12a_1^1 13a_1^2 3b_1^1 4b_1^1 5b_1^0 3b_2^2 4b_2^1 1a_2^1$	2.61		
$^7B_2$	$10a_1^2 11a_1^1 12a_1^1 13a_1^2 3b_1^2 4b_1^1 5b_1^0 3b_2^1 4b_2^1 1a_2^1$	2.61		
Linear MnC_2				
$^6A_1$	$10a_1^2 11a_1^1 12a_1^1 13a_1^0 3b_1^2 4b_1^1 5b_1^0 3b_2^2 4b_2^1 1a_2^1$	2.76		
$^6A_2$	$10a_1^1 11a_1^1 12a_1^0 13a_1^1 3b_1^2 4b_1^1 5b_1^0 3b_2^2 4b_2^1 1a_2^2$	5.78		
$^6B_1$	$10a_1^2 11a_1^1 12a_1^1 13a_1^1 3b_1^2 4b_1^0 5b_1^0 3b_2^2 4b_2^1 1a_2^1$	3.59		
$^6B_2$	$10a_1^2 11a_1^1 12a_1^1 13a_1^1 3b_1^2 4b_1^1 5b_1^0 3b_2^2 4b_2^0 1a_2^1$	3.59		
$^8A_1$	$10a_1^1 11a_1^1 12a_1^1 13a_1^1 3b_1^2 4b_1^1 5b_1^0 3b_2^2 4b_2^1 1a_2^1$	3.11		
$^8A_2$	$10a_1^1 11a_1^1 12a_1^1 13a_1^1 3b_1^2 4b_1^1 5b_1^1 3b_2^1 4b_2^1 1a_2^1$	6.55		
$^8B_1$	$10a_1^2 11a_1^1 12a_1^1 13a_1^1 3b_1^1 4b_1^1 5b_1^0 3b_2^2 4b_2^1 1a_2^1$	3.82		
$^8B_2$	$10a_1^2 11a_1^1 12a_1^1 13a_1^1 3b_1^2 4b_1^1 5b_1^0 3b_2^1 4b_2^1 1a_2^1$	3.82		

results of a $^6A_1$ ground state of the cyclic isomer [22]. It is indeed distinctively lower in energy by more than an eV than the $^8A_1$. The Mn–C and C–C bond lengths of the ground state are estimated to be 1.980 Å and 1.272 Å. The $^6A_1$ ($^6\Sigma^+$) of the linear MnC_2 isomer with M–C and C–C bond distances of 1.826 Å and 1.268 Å is placed at 0.45 eV above the ground state. For the anionic cluster, the $^7A_1$ state of the cyclic cluster appears as the ground state. Of interest for the assignment of the photoelectron spectra, the Mn–C distances of this state is calculated to be 2.094 Å, which is notably larger by 0.114 Å than the corresponding bond length of the neutral ground state. Also quite interestingly, the C–C bond distance hardly changes between the two ground states, it is reduced by just 0.008–1.264 Å. The $^5A_1$ state of the same isomer is calculated to be around 0.30 eV higher. For the linear structure, the $^5\Sigma^+$ ($^5A_1$) and $^7\Sigma^+$ ($^7A_1$) states are located at 0.24 eV and 0.27 eV above the $^7A_1$ of cyclic structure, respectively. Because these energy differences are rather small and certainly within the expected error bar of the DFT method, more elaborate calculations with wavefunction methods, such as CASPT2 and RCCSD(T) are undoubtedly needed.

CASPT2 geometric parameters and relative energies of low-lying states of $MnC_2^{-/0}$ clusters are collected in the middle part of Table 1. The corresponding leading configurations can be seen in Table 2. The latter table is included because it allows to identify without any doubt the electronic states that are relevant for the interpretation of the photoelectron spectra. Compared to the B3LYP relative energies there are some similarities but also some large differences. As a confirmation of the DFT results, CASPT2 predicts the $^7A_1$ state of cyclic MnC_2^- as the anionic global minimum. However, the $^5A_1$ state of the same isomer, which was computed to be 0.30 eV higher by B3LYP, is now estimated to be much higher in energy at 0.65 eV. For the linear structure, the $^7\Sigma^+$ ($^7A_1$) is 0.37 eV higher than the global minimum at this level of computation. Quite spectacularly, the relative energy of the $^5\Sigma^+$ ($^5A_1$) is shifted from the 0.24 eV B3LYP value to as much as 0.70 eV, which makes that the $^7\Sigma^+$ ($^7A_1$) becomes the lowest electronic state of the linear anionic structure. CASPT2 calculations for the neutral cluster reconfirm the $^6A_1$ of the cyclic structure as the ground state. New compared to the DFT results, the first excited state of this isomer is identified as the lower spin state of the same configuration as the $^8A_1$ (see Table 2). This 2^6A_1 state, which is inaccessible by B3LYP, is calculated by CASPT2 to be 0.72 eV higher than the $^6A_1$ state and will appear to be crucial for the assignment of the photoelectron spectra. The $^8A_1$ high-spin state is located just 0.03 eV higher than the 2^6A_1, which is the outcome of a pronounced configuration interaction for the latter state as testified by the composition of the CASSCF wavefunction. Our CASPT2 calculations also find $^6\Sigma^+$ and $^8\Sigma^+$ states of the linear isomer which are evaluated to be 0.76 eV and 1.03 eV higher than the $^6A_1$ global minima of the MnC_2 potential energy surface. Compared to B3LYP and without any exception, CASPT2 shifts the relative positions of the linear states with respect to the corresponding anionic and neutral ground states, to higher energies. Of importance for the photoelectron spectroscopy are the observed trends of the CASPT2 geometries between the anion ground state $^7A_1$ and the three lowest neutral states: $^6A_1$, $^8A_1$ and 2^6A_1. For the two former neutral states the same Mn–C bond variations (shortening for $^6A_1$ and elongation for $^8A_1$ and as good as unaffected C–C bonds, completely in agreement with B3LYP, are observed. The CASPT2 geometry for 2^6A_1 is the only one at our disposal for this state in this study, since the other two computational methods employed are unable to calculate it. As can be seen in the middle part of Table 1 both the Mn–C and C–C bond distances change by less than 0.01 Å between the $^7A_1$ anionic ground state and the 2^6A_1 excited neutral state.

The pseudo-natural orbitals and natural occupation numbers for the $^7A_1$ state of the cyclic structure as obtained by CASSCF are depicted in Figure 2. All singly occupied orbitals of the leading configuration of this ground state are either predominantly 3d orbitals or a hybrid 4s4p orbital of manganese: $10a_1$ ($d_{x^2-y^2}$), $11a_1$(d_{z^2}), $12a_1$ (4s4p), $4b_1$ (d_{xz}), $5b_2$ (d_{yz}), and $1a_2$ (d_{xy}). In respect to the Mn–C bonds, $5b_2$ and $4b_1$ show σ and π antibonding interaction, respectively. The other metal orbitals are dominantly ($11a_1$ and $12a_1$) or almost exclusively ($10a_1$ and $1a_2$) nonbonding orbitals. Apparently, the splittings between the nonbonding and antibonding valence metal orbitals are not large enough and the resulting equal distribution of the electrons with parallel spins gives rise to the high-spin $^7A_1$ ground state. The remaining eight active orbitals exhibit predominantly ligand character. Of these the $7a_1$ (σ(2s2p)), $4b_2$ (σ*(2s2p)), $9a_1$ (2s2p), $3b_1$ (π_x) and $8a_1$ (π_y) orbitals are doubly occupied, whereas $6b_2$ (π_y^*), $2a_2$(π_x^*) and $7b_2$ (σ*(2s2p)) orbitals are unoccupied. This leading electronic configuration of the anionic $^7A_1$ ground state is consistent with a C_2^{2-} coordinated ligand which exhibits 2s2p hybridization in its orbitals. This finding combined with the small covalent mixing that is seen in the CASSCF orbitals of Figure 2, leads to the conclusion

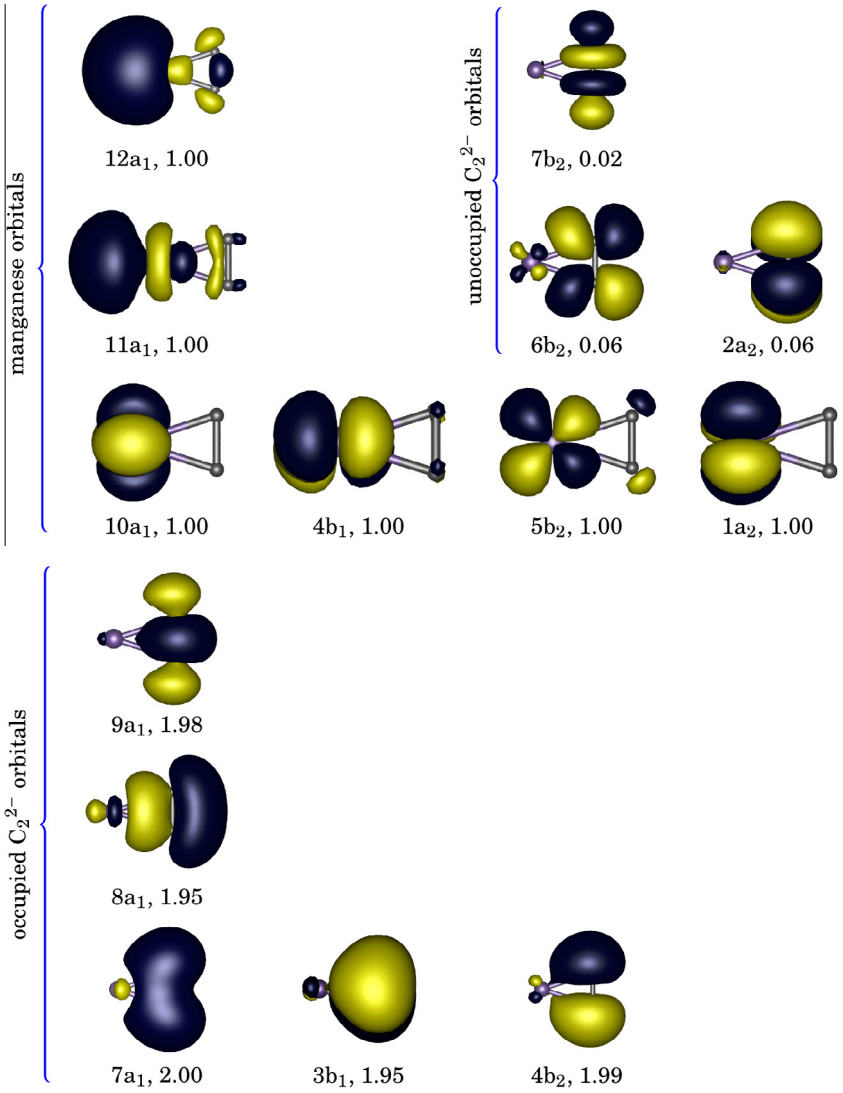

Figure 2. Pseudo-natural CASSCF molecular orbitals and occupation numbers of the $^7A_1$ state of cyclic MnC_2^-. Orbitals are grouped according to symmetry, predominant character and occupation in the leading configuration.

that the bonding in this complex is to a large extent an electrostatic interaction between the formally doubly negatively charged C_2^{2-} and Mn^+. The neutral $^6A_1$ ground state that is formed by the removal of an electron from the singly occupied $12a_1$ (4s4p) orbital of $^7A_1$, can be described by the oxidation state scheme $Mn^{+2}C_2^{-2}$. Further on, the principle electronic configuration of the 2^6A_1 and $^8A_1$ neutral states are the result of the detachment of an electron from the doubly occupied $9a_1$ (predominantly ligand HOMO) of $^7A_1$. Consequently, both states correspond to the scheme $Mn^+C_2^{-2}$. Also, because of their identical leading configuration the 2^6A_1 can be expected to have a higher energy than the high-spin $^8A_1$ state. Surprisingly, CASPT2 calculates 2^6A_1 as 0.03 eV more stable than $^8A_1$. The reason for this calculated stabilization of the 2^6A_1 is the strong electron configuration interaction of this state with other higher lying excited $^6A_1$ states of which some are of the same electronic configuration. All these observations are important for understanding the anion photoelectron spectra.

In Figure 3, the CASSCF molecular orbitals and occupation numbers for the lowest energy $^7\Sigma^+$ state of the linear isomer are depicted. Similar to the $^7A_1$ state of the cyclic isomer, all the predominant metal molecular orbitals are singly occupied. The $11a_1$ and $1a_2$ orbitals are d_δ nonbonding orbitals, $4b_1$ and $4b_2$ are d_π antibonding orbitals, $12a_1$ is d_σ nonbonding orbital and $13a_1$ is a nonbonding orbital with mainly contribution of the 4s4p hybrid orbital on Mn. Similar plots for the $^6\Sigma^+$ state show that the ionization $^7\Sigma^+ \rightarrow {}^6\Sigma^+$ is the result of the detachment of an electron from the $13a_1$ orbital. Additionally, in Figure 3 it can be seen that the three bonding orbitals with large contributions on the ligand, i.e. the $10a_1$ (σ), $3b_1$ (π) and $3b_2$ (π), are doubly occupied. The remaining ligand orbitals ($14a_1$, $5b_1$ and $5b_2$) are high-lying unoccupied C_2^{2-} antibonding orbitals. The computed occupation numbers lead to the same oxidation schemes for the linear $MnC_2^{-/0}$ ground states as for their cyclic counterparts, namely $Mn^{+1}C_2^{-2}$ for $^7\Sigma^+$ and $Mn^{+2}C_2^{-2}$ for $^6\Sigma^+$. The $^8\Sigma^+$ state is formed by electron detachment from the doubly occupied $10a_1$ orbital that is mainly localized on C_2^{2-}.

Based on the vital electronic structure information achieved from the CASSCF wavefunction analysis, as presented in the two previous paragraphs, it was possible to perform RCCSD(T) calculations for the relevant low-lying states of $MnC_2^{-/0}$. Correlation consistent triple-ζ basis sets were used for geometry optimizations, while the quintuple-ζ basis sets were employed for single point calculations with the aim to improve the relative energies. These type of calculations are needed because CASPT2 is known to predict wrong relative stabilities for the low-lying isomers for similar transition metal containing clusters, whereas RCCSD(T) was

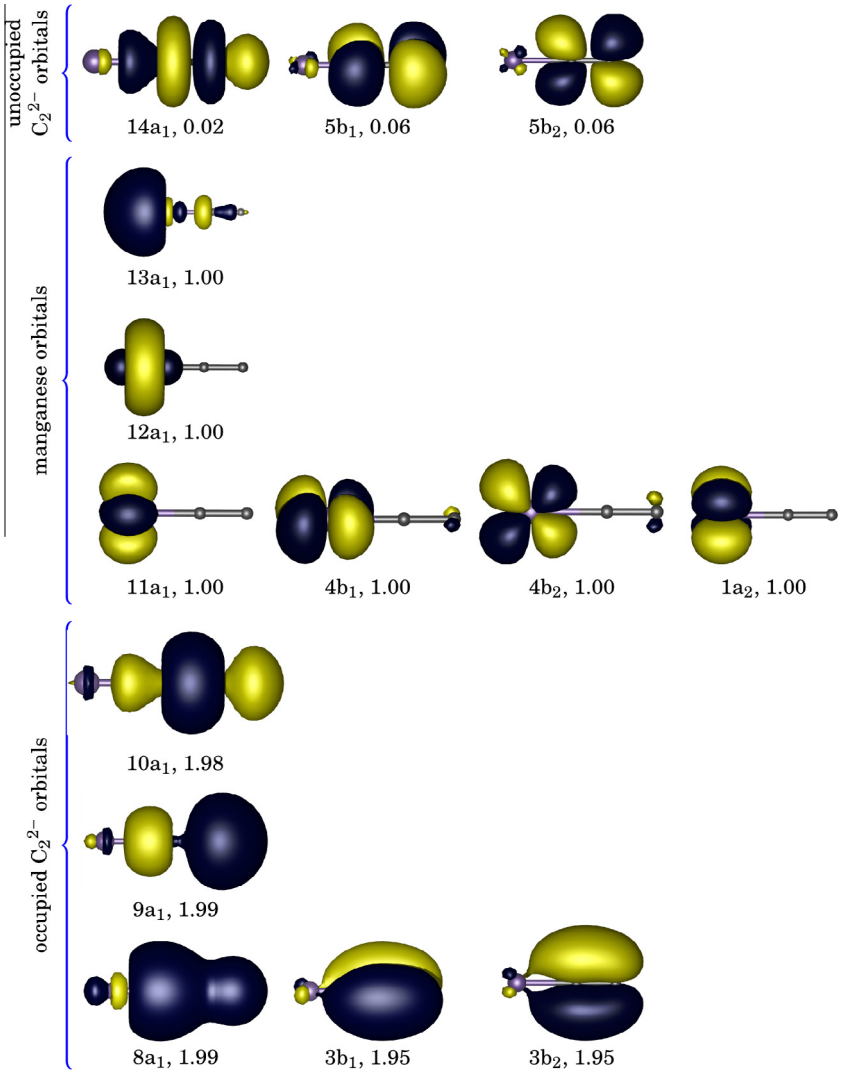

Figure 3. Pseudo-natural CASSCF molecular orbitals and occupation numbers of the $^7A_1$ state of linear MnC_2^-. The manganese atom is situated at the left hand side of the cluster. Orbitals are grouped according to symmetry, predominant character and occupation in the leading configuration.

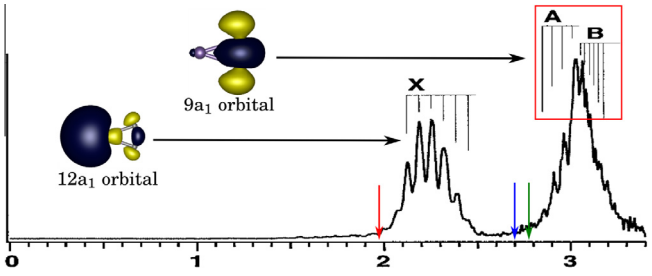

Figure 4. Photoelectron spectrum of MnC_2^- as measured with 355 nm photon energy [9]. The red, blue and green arrows represent CASPT2 adiabatic detachment energies for the $^7A_1 \rightarrow {}^6A_1$ (X band), $^7A_1 \rightarrow 2^6A_1$(A band) and $^7A_1 \rightarrow {}^8A_1$ (B band) ionizations, respectively. (For interpretation of the references to colour in this figure legend, the reader is referred to the web version of this article.)

demonstrated to be superior in this respect [25,26]. As shown in the lower part of Table 1, for the anionic cluster, our RCCSD(T) computations predict the $^7A_1$ of the cyclic isomer as the global minimum. As the CASSCF calculations revealed a very strong multireference wavefunction for the $^5A_1$ state of the same isomer, it turned out to be impossible to perform single-reference RCCSD(T) computations for this state, which is the reason as to why there is no entrance for this state in the lower part of Table 1. $^7\Sigma^+$ and $^5\Sigma^+$ states of the linear isomer are calculated to be 0.39 and 0.94 eV higher than the $^7A_1$ ground state, respectively. The $^6A_1$ state of cyclic conformation is computed to be the ground state of the neutral cluster, while the $^7\Sigma^+$ state of the linear isomer is 0.65 eV less stable. The $^8A_1$ and $^8\Sigma^+$ states of cyclic and linear isomers are placed at 0.75 and 1.15 eV above the $^6A_1$ state, respectively. Overall, the RCCSD(T) method provides the same picture as DFT and CASPT2. Therefore, and beyond any doubt, the $^7A_1$ of cyclic isomer must be seen as the initial state for the interpretation of the photoelectron spectra of MnC_2^-.

The photoelectron spectra of MnC_2^- were measured with photon energies of 532 and 355 nm, of which the latter spectrum is shown in Figure 4 [9]. Of the three bands that are observed only the lowest band (X), beginning at 2.12 eV, shows a clear vibrational progression with peak interspacings of 520 (30) cm^{-1}. The interpretation for the second feature in the spectrum is certainly less obvious. Pure on experimental evidence it was proposed as being composed of two vibrational progressions. The lowest band of these two (A band) commences at 2.86 eV and has a vibrational progression of 450 (40) cm^{-1}. The higher vibrational progression (B band) starting at 3.06 eV, and which overlaps with the A band, is proposed to possess a smaller frequency of 330 (40) cm^{-1}. In the following

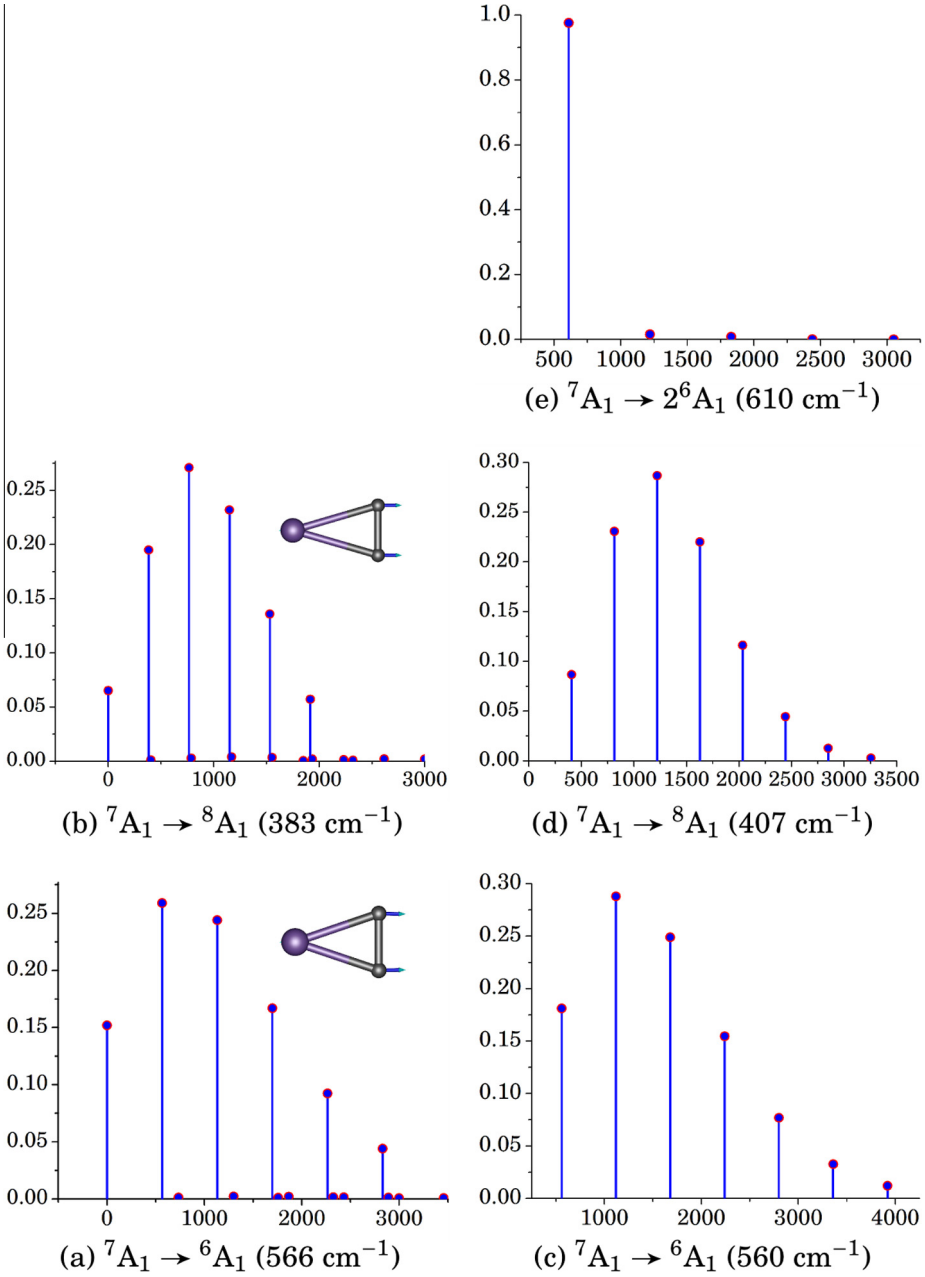

Figure 5. Franck–Condon factors as calculated from B3LYP harmonic vibrational analyses (a) and (b) and a CASPT2 simulation of the symmetric Mn–C_2 stretching mode (c), (d), and (e).

discussion, assignments of all these low-lying bands in the spectra will be proposed on the basis of the CASPT2 and RCCSD(T) computed ionization energies and multidimensional Franck–Condon factors obtained at the B3LYP and CASPT2 level of computation.

The lowest band in the anion photoelectron spectra is assigned to the $^7A_1 \rightarrow {}^6A_1$ transition. The adiabatic detachment energies (ADE's) as evaluated by CASPT2 and RCCSD(T), and collected in Table 1, are 1.98 and 2.18 eV, which correspond very well with the experimental electron binding energy for the X band of 2.12 eV. The CASPT2 vertical detachment energy (VDE) for this transition in Table 2 amounts to a value of 2.10 eV, which is somewhat larger than the CASPT2 ADE, as can be expected. The CASSCF orbital analysis as discussed in a previous paragraph allows to identify this ionization as a one-electron detachment out of the nonbonding $12a_1$ orbital, which is in essence a lone pair (4s4p hybrid) orbital on manganese. For the vibrational overlapping A and B bands at 2.86 eV and 3.06 eV, CASPT2 points to $^7A_1 \rightarrow 2^6A_1$ and $^7A_1 \rightarrow {}^8A_1$ transitions with computed ADEs of 2.70 eV and 2.73 eV, respectively. Both of these ionizations are the result of the removal of an electron (with different spin) from the doubly occupied bonding $9a_1$ orbital which is mainly located on the C_2^{2-} ligand. Because CASPT2 places the 2^6A_1 state slightly lower in energy by 0.03 eV than $^8A_1$, the $^7A_1 \rightarrow 2^6A_1$ is assigned to the A band and the $^7A_1 \rightarrow {}^8A_1$ to the B band. The large energy difference between the X band and the two other bands of about 0.75 eV, which is definitely larger than the expected error bar of the computational methods, permits to conclude that there is no uncertainty concerning the assignment of the former band. On the contrary, the experimental splitting between the A and B bands of 0.2 eV and the calculated CASPT2 energy difference of 0.03 eV between 2^6A_1 and $^8A_1$ are both smaller than the error bar of the employed computational method. Therefore, CASPT2 energies do not allow definite assignments for these

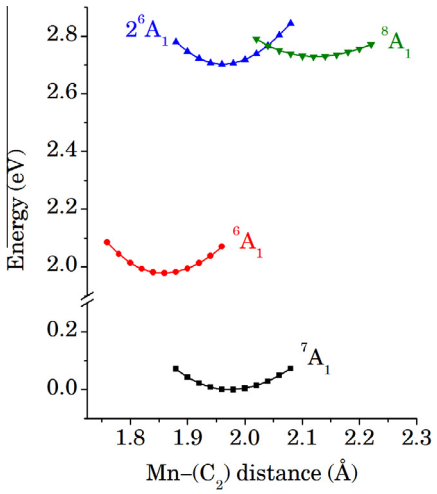

Figure 6. The potential energy profiles for the Mn–(C_2) stretching mode as obtained by CASPT2.

bands. In an attempt to reach a more final assignment, the additional experimental information provided by the observed vibrational progressions can be used by comparing them to Franck–Condon simulations for these three bands.

Figure 5 presents the Franck–Condon factors for the lowest ionizations of the cyclic MnC_2^- at B3LYP and CASPT2 levels. The B3LYP Franck–Condon factors are calculated by using the corresponding optimized structures, vibrational frequencies, and vibrational normal coordinates. The insets in Figure 5a and b show the vibrational mode that is responsible for the progression. For both ionizations the spectroscopic active mode appears to be a symmetric Mn–(C_2) stretching with hardly any mixing of the symmetric C–C stretching mode. For the ionization to the $^6A_1$ neutral ground state (Figure 5a), the frequency of this active mode is according to Table 1 evaluated as 566 cm^{-1}. That only this symmetric mode causes a progression is the outcome of the fact that this ionization is accompanied by a substantial decrease of the Mn–C bond distances from 2.094 Å for $^7A_1$ to 1.980 Å for $^6A_1$, while the C–C bond-length just slightly changes from 1.264 to 1.272 Å. By comparing the relative values of the Franck–Condon factors for this ionization in Figures 5a with the experimental vibrational progression of the X band in Figure 4, we can observe a nearly perfect match. Also, the calculated frequency of 566 cm^{-1} is in reasonable agreement with the experimental value of 520 (30) cm^{-1}. Our vibrational simulation for the $^7A_1 \rightarrow {}^8A_1$ ionization in Figure 5b shows a progression in which again only the symmetric Mn(C_2) stretching is active. Again this ionization is accompanied by a small decrease of the C–C bond length from 1.264 Å to 1.258 Å, whereas the Mn–C bond distances extensively increase from 2.094 Å to 2.247 Å. The computed frequency of 383 cm^{-1} for the Mn–(C_2) stretching agrees acceptably well with the experimental proposed value of 334 (40) cm^{-1}. Since B3LYP is not be able to calculate the excited 2^6A_1 state, it is impossible to perform a Franck–Condon factor simulation for the $^7A_1 \rightarrow 2^6A_1$ transition at this computational level. Fortunately, 2^6A_1 is accessible for CASPT2 and therefore the simulation will be carried out by using this method.

From the B3LYP harmonic vibrational analysis in the previous paragraph, we know that only the symmetric Mn–(C_2) stretching mode is active in the photoelectron spectra. Based on this information, manual CASPT2 harmonic vibrational analyses for this mode were performed. The potential energy profiles of the low-lying states for this mode were constructed by changing the Mn–(C_2) distance, while freezing the C–C bond-length at the CASPT2 optimized value. From the computed potential energy curves, which are depicted in Figure 6, we can conclude that the Mn–(C_2) distance adjusts from 1.974 Å for $^7A_1$ to 1.859 Å for $^7A_1$ and 2.213 Å for $^8A_1$. The Franck–Condon factors calculated at this level of theory for $^7A_1 \rightarrow {}^6A_1$ and $^7A_1 \rightarrow {}^8A_1$, as presented in Figure 5c and d, are in good agreement with the DFT results and with the vibrational progressions of the X and B bands. The corresponding CASPT2 vibrational frequencies for $^7A_1$, $^6A_1$ and $^8A_1$ are 488 cm^{-1}, 560 cm^{-1} and 407 cm^{-1}, respectively. They do not deviate much from the B3LYP frequencies of 474, 566, and 383 cm^{-1}. For 2^6A_1, the calculated CASPT2 frequency has a value of 610 cm^{-1} which is larger than the experimental proposed vibrational progression of 450 cm^{-1} for the A band. It is, however, also larger than the corresponding frequency of the $^8A_1$ state (383 cm^{-1}), which constitutes an indication to assign the $^7A_1 \rightarrow 2^6A_1$ ionization to the A band. Indeed, this band is experimentally proposed to exhibit a larger frequency than the B band (330 cm^{-1}). Furthermore, it corroborates the assignment made on the basis of the CASPT2 energies in a previous paragraph. Quite remarkably, the Franck–Condon simulation for this transition in Figure 5e exhibits only one peak. This result is in contrast with the experimental interpretation of the overlapping A and B bands. The lack of vibrational progression is the result of the similarity of the calculated Mn–(C_2) distances, i.e. 1.974 for $^7A_1$ and 1.962 Å for 2^6A_1. However, it was already mentioned that the 2^6A_1 has a very strong multireference character with large contributions of the $^6A_1$ ground state and the other six higher lying $^6A_1$ states of the same electronic configuration. This fact makes this state extremely difficult to calculate. Additionally, we feel that the experimental interpretation of the broad experimental band between 2.8 eV and 3.3 eV is subjected to a degree of uncertainty. Obviously, the interpretation of the A and the B bands of the experimental photoelectron spectra remains a challenge, both to experiment and theory.

4. Conclusion

The electronic structures of the two lowest isomers of $MnC_2^{-/0}$, namely cyclic and linear $MnC_2^{-/0}$, were investigated by DFT, CASPT2, and RCCSD(T). Our calculations at all levels show that the ground states of the anionic and neutral clusters are the $^7A_1$ and $^6A_1$ states of the cyclic isomer, respectively. Analyses of the CASSCF orbitals demonstrate that all valence orbitals of manganese, i.e. the 3d orbitals and the 4s4p hybrid, are singly occupied for the $^7A_1$ state, whereas the 4s4p hybrid is unoccupied in the case of $^6A_1$. The nature of the doubly occupied valence orbitals allows to identify the ligand as formally a double negatively charged C_2^{2-}. Therefore, the oxidation state of manganese is either +1 for the anionic or +2 for the neutral cluster, respectively. For the first time ever an assignment for the photoelectron spectra is proposed. The CASPT2 calculations allowed to account for all observed bands in the experimental photoelectron spectra of MnC_2^- by using the cyclic $^7A_1$ ground state as the initial state. With certainty, the X band can be ascribed to $^7A_1 \rightarrow {}^6A_1$, corresponding to an ionization out of the 4s4p nonbonding hybrid orbital on manganese. The assignment of the remaining two experimental bands is to some extent tentative. The CASPT2 relative energies and vibrational frequencies suggest that the A band corresponds to the $^7A_1 \rightarrow 2^6A_1$ ionization and the B band to the $^7A_1 \rightarrow {}^8A_1$ transition. However, beyond any doubt both bands correspond to electron detachments from the HOMO of the C_2^{2-} ligand. The calculated multidimensional Franck–Condon factors for the $^7A_1 \rightarrow {}^6A_1$ and $^7A_1 \rightarrow {}^8A_1$ transitions at the B3LYP and CASPT2 levels successfully reproduce the vibrational progressions of the X and B bands in the spectra.

References

[1] D.S. Bethune, R.D. Johnson, J.R. Salem, M.S. Devries, C.S. Yannoni, Nature 366 (1993) 123.
[2] B.C. Guo, K.P. Kerns, A.W. Castleman, Science 255 (1992) 1411.
[3] B.C. Guo, S. Wei, J. Purnell, S. Buzza, A.W. Castleman, Science 256 (1992) 515.
[4] S. Li, H.B. Wu, L.S. Wang, J. Am. Chem. Soc. 119 (1997) 7417.
[5] H. Shinohara, Rep. Prog. Phys. 63 (2000) 843.
[6] S.A. Bates, J.A. Rhodes, C.M.L. Rittby, W.R.M. Graham, J. Chem. Phys. 127 (2007) 064506.
[7] S.A. Bates, C.M.L. Rittby, W.R.M. Graham, J. Chem. Phys. 125 (2006) 074506.
[8] D.G. Dai, S. Roszak, K. Balasubramanian, J. Phys. Chem. A 104 (2000) 9760.
[9] X. Li, L.S. Wang, J. Chem. Phys. 111 (1999) 8389.
[10] S. Roszak, D. Majumdar, K. Balasubramanian, J. Chem. Phys. 116 (2002) 10238.
[11] K. Tono, A. Terasaki, T. Ohta, T. Kondow, J. Chem. Phys. 117 (2002) 7010.
[12] L.S. Wang, X. Li, J. Chem. Phys. 112 (2000) 3602.
[13] H.J. Zhai, S.R. Liu, X. Li, L.S. Wang, J. Chem. Phys. 115 (2001) 5170.
[14] H.J. Zhai, L.S. Wang, P. Jena, G.L. Gutsev, C.W. Bauschlicher, J. Chem. Phys. 120 (2004) 8996.
[15] M.F.A. Hendrickx, S. Clima, Chem. Phys. Lett. 388 (2004) 290.
[16] M.F.A. Hendrickx, S. Clima, Chem. Phys. Lett. 388 (2004) 284.
[17] D. Majumdar, S. Roszak, K. Balasubramanian, J. Chem. Phys. 118 (2003) 130.
[18] R. Sumathi, N. Hendrickx, Chem. Phys. Lett. 287 (1998) 496.
[19] A.V. Arbuznikov, M. Hendrickx, L.G. Vanquickenborne, Chem. Phys. Lett. 310 (1999) 515.
[20] A.V. Arbuznikov, M. Hendrickx, Chem. Phys. Lett. 320 (2000) 575.
[21] V.M. Rayón, P. Redondo, C. Barrientos, A. Largo, J. Phys. Chem. A 111 (2007) 6345.
[22] V.M. Rayón, P. Redondo, C. Barrientos, A. Largo, Chem. Eur. J. 12 (2006) 6963.
[23] Y.B. Yuan, K.M. Deng, Y.Z. Liu, C.M. Tang, Chin. Phys. Lett. 23 (2006) 1761.
[24] V.T. Tran, M.F.A. Hendrickx, J. Phys. Chem. A 115 (2011) 13956.
[25] V.T. Tran, M.F.A. Hendrickx, J. Chem. Phys. 135 (2011) 094505.
[26] V.T. Tran, M.F.A. Hendrickx, J. Chem. Theory Comput. 7 (2011) 310.
[27] A.D. Becke, Phys. Rev. A 38 (1988) 3098.
[28] A.D. Becke, J. Chem. Phys. 98 (1993) 5648.
[29] C.T. Lee, W.T. Yang, R.G. Parr, Phys. Rev. B 37 (1988) 785.
[30] F. Weigend, F. Furche, R. Ahlrichs, J. Chem. Phys. 119 (2003) 12753.
[31] H.-J. Werner, P.J. Knowles, F.R. Manby, M. Schütz, et al., MOLPRO, version 2009.1, a package of ab initio programs <http://www.molpro.net>.
[32] R. Borrelli, A. Peluso, J. Chem. Phys. 119 (2003) 8437.
[33] B.O. Roos, R. Lindh, P.-Å. Malmqvist, V. Veryazov, P.O. Widmark, J. Phys. Chem. A 109 (2005) 6575.
[34] B.O. Roos, R. Lindh, P.-Å. Malmqvist, V. Veryazov, P.O. Widmark, J. Phys. Chem. A 108 (2004) 2851.
[35] Y. Ishikawa, M.J. Vilkas, J. Mol. Struct.-Theochem 573 (2001) 139.
[36] M. Reiher, A. Wolf, J. Chem. Phys. 121 (2004) 10945.
[37] M. Reiher, A. Wolf, J. Chem. Phys. 121 (2004) 2037.
[38] G. Karlström et al., Comp. Mater. Sci. 28 (2003) 222.
[39] N.B. Balabanov, K.A. Peterson, J. Chem. Phys. 123 (2005) 064107.
[40] R.A. Kendall, T.H. Dunning, R.J. Harrison, J. Chem. Phys. 96 (1992) 6796.